TECHNICAL MEMORANDUM

705

Representing equilibrium and non-equilibrium convection in large-scale models

P. Bechtold, N. Semane, P. Lopez, J.-P. Chaboureau*, A. Beljaars, N. Bormann

Research Department

* Laboratoire d'Aérologie, University of Toulouse and CNRS, Toulouse

Submitted to J. Atmos. Sci. The definitive version will be published by the Americ. Meteorol. Soc.

September 12, 2013

European Centre for Medium-Range Weather Forecasts
Europäisches Zentrum für mittelfristige Wettervorhersage
Centre européen pour les prévisions météorologiques à moyen terme

Series: ECMWF Technical Memoranda

A full list of ECMWF Publications can be found on our web site under:
http://www.ecmwf.int/publications/

Contact: library@ecmwf.int

European Centre for Medium-Range Weather Forecasts
Shinfield Park, Reading, RG2 9AX, England

Abstract

A new diagnostic convective closure, which is dependent on the convective available potential energy (*CAPE*), is derived under the quasi-equilibrium assumption for the free troposphere subject to boundary-layer forcing. The closure involves a convective adjustment time-scale for the free troposphere, and a coupling coefficient between the free troposphere and the boundary-layer based on different time-scales over land and ocean. Earlier studies with the ECMWF Integrated Forecasting System (*IFS*) have already demonstrated the model's ability to realistically represent tropical convectively-coupled waves and synoptic variability with use of the 'standard' *CAPE* closure, given realistic entrainment rates.

A comparison of low-resolution seasonal integrations and high-resolution short-range forecasts against complementary satellite and radar data shows that with the extended *CAPE* closure it is also possible, independently of model resolution and time step, to realistically represent non-equilibrium convection such as the diurnal cycle of convection and the convection tied to advective boundary-layers, though representing the late night convection over land remains a challenge. A more in depth regional analysis of the diurnal cycle and the closure is provided for the continental United States and particularly Africa, including comparison with data from satellites and a cloud resolving model (*CRM*). Consequences for global numerical weather prediction (*NWP*) are not only a better phase representation of convection, but also better forecasts of its spatial distribution and local intensity.

1 Introduction

Equilibrium convection is generally interpreted as indicating that the convection is in equilibrium with the forcing due to the mean advection and processes other than convection. In other words, the convection can react on time scales short enough for the residual tendency between the forcing and the convective stabilization to be small as measured by some function such as the cloud work function or the convective available potential energy (CAPE) (Arakawa and Schubert, 1974). This is generally referred to as quasi-equilibrium. Numerous theoretical and experimental studies (e.g. Emanuel et al., 1994; Neelin and Yu, 1994; Craig, 1996; Jones and Randall, 2011; Yano and Plant, 2012) have confirmed the validity of quasi-equilibrium for synoptic disturbances and for time-scales of the order of one day. However, various studies (Emanuel, 1993a; Raymond, 1995; Zhang, 2002; Donner and Philips, 2003; Raymond and Herman, 2011) have pointed out that the adjustment in the boundary-layer occurs on much shorter time-scales than that in the free troposphere.

Today most global numerical weather prediction (NWP) and climate models employ a convection parametrization scheme based on the concept that vertical mass transport occurs in convective plumes which exchange mass with their environment. In these schemes the rate of horizontal mass exchange has to be specified, and the mass flux at cloud base is determined from the assumption of convective quasi-equilibrium. A non-exhaustive list of basic parametrization schemes used in these models includes Arakawa and Schubert (1974), Bougeault (1985), Tiedtke (1989), Gregory and Rowntree (1990), Emanuel (1993b), Kain and Fritsch (1993), Zhang and McFarlane (1995), though many of these schemes have later been substantially modified and improved. In spite of employing a similar basic convective framework, the models can produce substantially different large-scale tropical wave spectra and intra-seasonal variability such as the Madden-Julian oscillation (Lin et al., 2006; Kim et al., 2011; Blackburn et al., 2013; Benedict et al., 2013). However, Bechtold et al. (2008), Vitart and Molteni (2009), Jung et al. (2010) and Hirons et al. (2013a) demonstrated with ECMWF's Integrated Forecasting System (IFS) that the basic mass flux framework under the quasi-equilibrium assumption provides a realistic reproduction of the observed middle-latitude synoptic variability, as well as the tropical wave spectra and intra-seasonal variability. In order to achieve this, two important properties of the convection scheme

were required, an adaptive adjustment time-scale for the CAPE, and a realistic strong entrainment rate (Derbyshire et al., 2004; de Rooy et al., 2013). The latter represents the observed heating modes from shallow, congestus and deep clouds in the tropics (Lin et al., 2012).

In contrast to equilibrium convection, the forcing of non-equilibrium convection varies typically on time scales of a few hours (Jones and Randall, 2011; Yano and Plant, 2012; Davies et al., 2013). Non-equilibrium convection under rapidly-varying forcing typically occurs when either the upper-tropospheric forcing is strong and the convection is inhibited by a capping inversion, or the upper-level forcing is weak and the precipitating convection is driven along its trajectory by rapidly-varying and strong surface heat fluxes. Note that the quasi-geostrophic adjustment process of a net heat source occurs via inertia-gravity waves on time-scales of a few hours. Forecasting non-equilibrium convection is challenging for models, and this is particularly true for surface-forced convection where the mesoscale adiabatic lifting/sinking couplet in the free troposphere is the response to and not the source of convective heating.

The diurnal cycle of convection is probably the most prominent manifestation of non-equilibrium convection driven by the boundary-layer. Numerous observational studies (e.g. Yang and Slingo, 2001; Dai et al., 1999; Tian et al., 2005; Zhang and Klein, 2010) and those based on cloud resolving models (CRMs) (e.g. Chaboureau et al., 2004; Khairoutdinov and Randall, 2006; Schlemmer et al., 2011) have been devoted to the diurnal cycle of convection over land. The phase of the diurnal cycle can strongly vary on regional scales, though the general picture is that of a morning shallow convective phase, followed by a gradual onset of deeper convection, with rain rates peaking in the late afternoon to early evening. It has been found that the phase and intensity of precipitation mainly depends on the surface fluxes and lower to mid-tropospheric stability and moisture, but boundary-layer processes such as convergence, gravity waves and cold pools also play a role in the onset and propagation of deep convection. It has been shown that CRMs with resolutions of order 2.5 km or higher are able to reproduce the observed diurnal cycle (e.g. Petch et al., 2002; Sato et al., 2008; Stirling and Stratton, 2012), but a strong resolution sensitivity exists with respect to both amplitude and phase for coarser horizontal resolutions when no convection parametrization is employed. However, Sato et al. (2009) and Marsham et al. (2013) have reasonably reproduced the observed phase in CRM-type simulations at 7 and 12 km horizontal resolutions, respectively.

The same success in reproducing the observed diurnal cycle can generally not be reported for large-scale models. Indeed, numerous global and regional model studies (Slingo et al., 1992; Dai et al., 1999; Betts and Jakob, 2002; Bechtold et al., 2004; Clark et al., 2007; Brockhaus et al., 2008; Stratton and Stirling, 2012; Langhans et al., 2013; Marsham et al., 2013) and comparisons of CRMs with single-column models (Guichard et al., 2004; Grabowski et al., 2006) pointed to systematic errors in the diurnal cycle of precipitation when a convection parametrization scheme is employed, namely a too early onset of deep convection with a diurnal cycle of precipitation that is roughly in phase with the surface fluxes. A notable exception are the successful simulations reported by Takayabu and Kimoto (2008). The diurnal cycle of non-precipitating shallow convection, however, can be realistically represented with a quasi-equilibrium closure for the boundary-layer and a prognostic cloud scheme, as demonstrated with the IFS by Ahlgrimm and Forbes (2012).

Various approaches have been taken to improve the representation of convection driven by surface fluxes. While Piriou et al. (2007), Del Genio and Wu (2010) and Stratton and Stirling (2012) focused on the entrainment rates, important work has also been done on convective closure as reviewed in Yano et al. (2013). In particular, Pan and Randall (1998) and Gerard et al. (2009) accounted for convective memory through a prognostic closure for the updraft kinetic energy and/or updraft area fraction. Mapes (2000), Rio et al. (2009) and Fletcher and Bretherton (2010) proposed convective closures involving the convective inhibition (CIN) and/or lifting by cold pools, while a humidity dependent closure has been adopted

in Fuchs and Raymond (2007). However, so far none of the above methods have proved to be general and robust enough to replace, at least in the global NWP context, the standard equilibrium closures for the CAPE or cloud work function. The notable exception being the studies by Donner and Philips (2003) and Zhang (2002) who evaluated the quasi-equilibrium assumption for CAPE against observations, whilst recognizing findings by Raymond (1995) on different adjustment time-scales for the free troposphere and the boundary-layer. From those studies it was concluded that it should be possible to formulate a CAPE closure for the free troposphere under a quasi-equilibrium assumption that also holds for rapidly-varying boundary-layer forcing.

The above considerations constitute the basis for the present article, where we derive a CAPE closure involving appropriate boundary-layer time-scales over land and water. Indeed, we show that with this extended diagnostic closure it is possible to represent not only large-scale synoptically driven convection, but also non-equilibrium boundary-layer driven convection with its characteristic diurnal cycle, and the inland advection of wintry convective showers. The article is organized as follows. The CAPE closure is derived in Section 2, followed in Section 3 by an evaluation against satellite and radar data of the diurnal cycle of convection in low-resolution seasonal integrations and high-resolution short-range forecasts. A more in depth discussion of the physics of the new closure and the diurnal cycle in the Sahel region, which makes use of complementary satellite and CRM data, is provided in Section 4. Conclusions and consequences for NWP are discussed in Section 5, including a brief discussion of a wintry convective situation under strong advection.

2 Convective closures

The convective available potential energy CAPE (J kg^{-1}) is defined as the buoyancy integral

$$\mathrm{CAPE} = g \int_{z_{\mathrm{base}}}^{z_{\mathrm{top}}} \frac{T_{\mathrm{v}}^{\mathrm{upad}} - \bar{T}_{\mathrm{v}}}{\bar{T}_{\mathrm{v}}} dz \approx g \int_{z_{\mathrm{base}}}^{z_{\mathrm{top}}} \frac{\theta_{\mathrm{e}}^{\mathrm{upad}}(T,q) - \theta_{\mathrm{esat}}(\bar{T})}{\theta_{\mathrm{esat}}(\bar{T})} dz, \tag{1}$$

where the integration in height coordinates z is between cloud base and cloud top, T_{v} is the virtual temperature and g gravity; the superscript 'upad' denotes values of an air parcel lifted pseudo-adiabatically, (i.e. without considering mixing with environmental air), and bars denote environmental or grid-mean values. For diagnostic purposes CAPE can be reasonably approximated by using the saturated equivalent potential temperature θ_{esat} instead of $\bar{T}_{\mathrm{v}}$, and the equivalent potential temperature $\theta_{\mathrm{e}}^{\mathrm{upad}}$, depending on temperature T and specific humidity q, instead of $T_{\mathrm{v}}^{\mathrm{upad}}$. As θ_{e} is conserved during moist adiabatic ascent, the rhs of (1) shows that the updraft thermodynamic properties are determined by the temperature and moisture in the departure layer of the rising air parcel that predominantly roots in the boundary-layer.

In the context of convection parametrization we use integration over pressure and define PCAPE (J m^{-3}) as the density weighted buoyancy integral of an entraining ascending air parcel

$$\mathrm{PCAPE} = -\int_{p_{\mathrm{base}}}^{p_{\mathrm{top}}} \frac{T_{\mathrm{v}}^{\mathrm{up}} - \bar{T}_{\mathrm{v}}}{T_{\mathrm{v}}} dp. \tag{2}$$

The entrainment rates used to compute $T_{\mathrm{v}}^{\mathrm{up}}$ are given in the Appendix. The advantage of PCAPE over an entraining CAPE is the density scaling that more readily relates the time derivative of PCAPE to the convective mass flux.

Under the assumption of vanishing updraft temperature excess at cloud top, and using $T_v^{up} - \bar{T}_v \ll \bar{T}_v$, the time derivative of PCAPE is obtained as

$$\frac{\partial \mathrm{PCAPE}}{\partial t} = \underbrace{\int_{p_{base}}^{p_{top}} \frac{1}{T_v} \frac{\partial \bar{T}_v}{\partial t} dp}_{\mathrm{LS+CONV}} \underbrace{- \int_{p_{base}}^{p_{top}} \frac{1}{T_v} \frac{\partial T_v^{up}}{\partial t} dp + \left. \frac{T_v^{up} - \bar{T}_v}{T_v} \right|_{base} \frac{\partial p_{base}}{\partial t}}_{\mathrm{BL+CONV}}. \tag{3}$$

The evolution of PCAPE includes production of PCAPE by radiative and advective large-scale processes (LS), and destruction of PCAPE by Cumulus convection (CONV), both affecting $\bar{T}_v$. Furthermore, there is production of PCAPE by boundary-layer (BL) processes other than convection, and removal by convective boundary-layer venting, and cooling by downdrafts and subcloud rain evaporation, all affecting T_v^{up}. The prognostic equation for PCAPE can then be formally rewritten as

$$\frac{\partial \mathrm{PCAPE}}{\partial t} = \left. \frac{\partial \mathrm{PCAPE}}{\partial t} \right|_{\mathrm{LS}} + \left. \frac{\partial \mathrm{PCAPE}}{\partial t} \right|_{\mathrm{BL}} + \left. \frac{\partial \mathrm{PCAPE}}{\partial t} \right|_{\mathrm{CONV=shal+deep}}. \tag{4}$$

Note that the CONV term contains both, the convective stabilization of the free troposphere (LS) and the boundary-layer (BL), it is the sum of the contributions from shallow and deep convection.

Similar prognostic equations for CAPE have also been derived in Zhang (2002) and Donner and Philips (2003).

The LS production term includes the tendencies due to mean vertical and horizontal advection and radiation, it is given by

$$\left. \frac{\partial \mathrm{PCAPE}}{\partial t} \right|_{\mathrm{LS}} = \int_{p_{base}}^{p_{top}} \left. \frac{1}{T_v} \frac{\partial \bar{T}_v}{\partial t} \right|_{\mathrm{adv+rad}} dp. \tag{5}$$

The tendency due to convection can either be approximated assuming that cumulus convection acts to remove PCAPE over a convective time scale τ (Fritsch and Chappell, 1980; Betts and Miller, 1986; Nordeng, 1994)

$$\left. \frac{\partial \mathrm{PCAPE}}{\partial t} \right|_{\mathrm{CONV,1}} = -\frac{\mathrm{PCAPE}}{\tau}, \tag{6}$$

or by approximating the convective tendency by the heating through compensating environmental subsidence, so that the convective mass flux M (kg m^{-2} s^{-1}) becomes apparent

$$\left. \frac{\partial \mathrm{PCAPE}}{\partial t} \right|_{\mathrm{CONV,2}} \approx - \int_{z_{base}}^{z_{top}} \frac{g}{T_v} M \left(\frac{\partial \bar{T}_v}{\partial z} + \frac{g}{c_p} \right) dz = - \frac{M_{base}}{M^*_{base}} \int_{z_{base}}^{z_{top}} \frac{g}{T_v} M^* \left(\frac{\partial \bar{T}_v}{\partial z} + \frac{g}{c_p} \right) dz, \tag{7}$$

with c_p the specific heat at constant pressure. The ratio between the actual (final) cloud base mass flux, and the unit (initial) cloud base mass flux M_{base}/M^*_{base} is the convective scaling or closure factor. The initial mass flux profile M^*, and initial cloud base mass flux M^*_{base} are known from the updraft computation.

Different convective closures can then be formulated on the basis of (4), keeping in mind that a mass flux scheme requires a closed expression for the cloud base mass flux M_{base}, therefore we need to retain (7).

If we know the boundary-layer (BL) term, PCAPE can be determined prognostically from (4) using (5) and (6). The convective mass flux is then obtained diagnostically from

$$\left.\frac{\partial \mathrm{PCAPE}}{\partial t}\right|_{\mathrm{CONV},2} = \left.\frac{\partial \mathrm{PCAPE}}{\partial t}\right|_{\mathrm{CONV},1} \tag{8}$$

Alternatively, in a purely diagnostic scheme we can compute PCAPE from (2), and again use (8) to compute the convective mass flux. Note that in this diagnostic formulation PCAPE implicitly contains the production from BL and LS.

Another diagnostic closure is obtained from (4) if we use (5) and (7), neglect the lhs and assume a boundary-layer in equilibrium

$$\left.\frac{\partial \mathrm{PCAPE}}{\partial t}\right|_{\mathrm{LS}} = -\left.\frac{\partial \mathrm{PCAPE}}{\partial t}\right|_{\mathrm{CONV},2}. \tag{9}$$

This relation is another formulation of the quasi-equilibrium between the large-scale destabilization and the convection, but as defined by the integral bounds, it is the quasi-equilibrium for the free troposphere. No time scale τ has to be specified, as it is implicitly contained in the LS tendency. However, experimentation shows that this closure is not general enough, as it underestimates convective activity in situations where the LS forcing is weak, and where convective heating precedes the dynamic adjustment.

Finally, even a suitable moisture convergence closure can be formulated that is consistent with (4) using (7)

$$\int_{p_{\mathrm{surf}}}^{p_{\mathrm{top}}} \left.\frac{\partial \bar{q}}{\partial t}\right|_{\mathrm{adv+BL}} dp = \left.\frac{\partial \mathrm{PCAPE}}{\partial t}\right|_{\mathrm{CONV},2}, \tag{10}$$

where the integration is from the surface to the top of the atmosphere including LS and BL. This closure, in spite of assuming moisture as a source of convection instead of instability, has properties of both (9) and (8). It is still applied in NWP (Bougeault, 1985), but tests with the IFS did not lead to optimal model performance.

2.1 Diagnostic CAPE closure

As outlined above, a convenient diagnostic CAPE closure can be defined using (8) and substituting for (7), (6) and computing PCAPE from (2). The cloud base mass flux is then obtained as

$$M_{\mathrm{base}} = M^*_{\mathrm{base}} \frac{PCAPE}{\tau} \frac{1}{\int_{z_{\mathrm{base}}}^{z_{\mathrm{top}}} \frac{g}{\bar{T}_{\mathrm{v}}} M^* \left(\frac{\partial \bar{T}_{\mathrm{v}}}{\partial z} + \frac{g}{c_p} \right) dz}. \tag{11}$$

Apart from using a density-weighted PCAPE instead of an entraining CAPE, this is the closure for the deep convective mass fluxes that has been used in the IFS since Gregory et al. (2000). With this formulation the convective mass flux closely follows the large-scale forcing and/or the surface fluxes when the CIN is small and the adjustment time-scale is reasonably short.

The closure (11) is complete with a definition of the convective adjustment time-scale τ following Bechtold et al. (2008)

$$\tau = \frac{H_{\mathrm{c}}}{\bar{w}^{\mathrm{up}}} f(n) = \tau_{\mathrm{c}} f(n); \qquad f(n) = 1 + \frac{264}{n} \tag{12}$$

Here, τ_c is the convective turnover time-scale with H_c the convective cloud depth, $\bar{w}^{up}$ is the vertically averaged updraft velocity, and f is an empirical scaling function decreasing with increasing spectral truncation (horizontal resolution) n. The minimum allowed value for τ is set to 12 minutes. Note that τ_c depends itself on PCAPE through $\bar{w}^{up}$ which is consistent with the observations by Zimmer et al. (2011). In the following the closure described by (11) and (12) is referred to as CTL.

2.2 Diagnostic CAPE closure with boundary-layer equilibrium

As the above closure (11) does not reproduce the observed diurnal cycle (as shown later), even when employing large entrainment rates in the convection scheme that are consistent with CRM data (Del Genio and Wu, 2010; de Rooy et al., 2013), it is suggested that it does not reproduce the observed non-equilibrium between the boundary-layer forcing and the deep convection. Zhang (2002) and Donner and Philips (2003) have shown through an analysis of observational data of middle-latitude and tropical convection that the assumption that $\partial \mathrm{PCAPE}/\partial t$ is small compared to the individual terms on the rhs of (4) is not valid if the boundary-layer is not in equilibrium. Indeed the boundary-layer production term is the dominant term in surface driven convection under weak large-scale forcing. To our knowledge, in most parametrizations using a CAPE-type closure, the imbalance between the deep convection and the BL production is not explicitly taken into account. However, some authors (e.g. Raymond, 1995) have taken an alternative approach by proposing separate boundary-layer equilibrium closures.

We define the total boundary-layer production in (4) as proportional to the surface buoyancy flux

$$\left.\frac{\partial \mathrm{PCAPE}}{\partial t}\right|_{\mathrm{BL}} = -\frac{1}{T_\star}\int_{p_{\mathrm{surf}}}^{p_{\mathrm{base}}} \left.\frac{\partial \bar{T}_v}{\partial t}\right|_{\mathrm{BL}} dp, \tag{13}$$

where $\partial \bar{T}_v/\partial t|_{\mathrm{BL}}$ includes the tendencies from mean advection, diffusive heat transport and radiation. In the model context these tendencies must be available before the convection is taken into account. The temperature $T_\star$ scales as $T_\star = c_p^{-1} gH$ with H a characteristic height. We have set $T_\star = 1\mathrm{K}$ and cast the scaling into the coefficient α below. In a prognostic scheme one could in principle formulate the boundary-layer contribution to be formally consistent with the 2nd term on the rhs of (3), the 3rd term being generally small. However, the BL contribution in (3) is the sum of the convective contribution and the forcing. In a model, the non-convective BL forcing could be isolated, by calculating the BL temperature tendency due to non-convective terms. Furthermore, the tendency of the updraft virtual temperature can be rather discontinuous in space and time, and even become negative while there is surface heating. Therefore, (13) is the preferred formulation of the boundary-layer contribution to PCAPE taking into account all relevant forcings.

In order to account for the imbalance between boundary-layer heating and deep convective overturning we write the convective tendency as the relaxation of an effective PCAPE

$$\left.\frac{\partial \mathrm{PCAPE}}{\partial t}\right|_{\mathrm{CONV=deep}} = -\frac{PCAPE}{\tau} + \alpha \left.\frac{\partial \mathrm{PCAPE}}{\partial t}\right|_{\mathrm{BL}}; \qquad \alpha = \frac{\tau_{\mathrm{bl}}}{\tau}, \tag{14}$$

with α the fraction of boundary-layer forcing consumed by shallow convection. α is given as the ratio of the boundary-layer time-scale τ_{bl} to the deep convective adjustment time-scale τ and can also be interpreted as a convective coupling coefficient between the free troposphere and the boundary-layer, with $\alpha = 0$ corresponding to a perfect coupling regime and $\alpha = 1$ to decoupling. The boundary-layer time-scale τ_{bl} should satisfy the dimensional form $[HU_\star^{-1}]$ with $U_\star$ a characteristic speed. It is set equal to the convective time-scale τ_c over land, assuming that the boundary-layer adjusts to deep convective heat

transport through the updrafts and downdrafts. Over water it is set to the horizontal advective time-scale, assuming a quasi-homogeneous oceanic boundary-layer in equilibrium

$$\begin{aligned} \tau_{\rm bl} &= \tau_{\rm c} \quad \text{land} \\ \tau_{\rm bl} &= \frac{H_{\rm base}}{\bar{u}_{\rm bl}} \quad \text{water}, \end{aligned} \tag{15}$$

where $H_{\rm base}$ is the cloud base height and $\bar{u}_{\rm bl}$ the average horizontal wind speed in the subcloud layer.

Setting $\partial \text{PCAPE}/\partial t = 0$ in (4) enforces essentially a balance between the second and third term of the rhs when the boundary-layer forcing dominates, and an equilibrium between the first and third term, when the boundary-layer is in equilibrium and the large-scale forcing dominates. Using (14) for the PCAPE consumption by deep convection and following the same procedure as used for deriving (11), the scaling for the deep convective cloud base mass flux can be written as

$$M_{\rm base} = M^*_{\rm base} \frac{PCAPE - PCAPE_{\rm bl}}{\tau} \frac{1}{\int_{z_{\rm base}}^{z_{\rm top}} \frac{g}{\bar{T}_{\rm v}} M^* \left(\frac{\partial \bar{T}_{\rm v}}{\partial z} + \frac{g}{c_p} \right) dz}; \quad M_{\rm base} \geq 0. \tag{16}$$

with

$$PCAPE_{\rm bl} = -\tau_{\rm bl} \frac{1}{T_\star} \int_{p_{\rm surf}}^{p_{\rm base}} \left. \frac{\partial \bar{T}_{\rm v}}{\partial t} \right|_{\rm BL} dp. \tag{17}$$

for convection rooting in the boundary-layer. For convection rooting above the boundary-layer $PCAPE_{\rm bl}$ is set to zero. The closure is equivalent to relaxing PCAPE toward a value $\text{PCAPE}_{\rm bl}$ instead of zero. It considers only the part of PCAPE that is due to free tropospheric production as long as the boundary-layer is not in equilibrium. The closure consists in substracting from the total mass flux a (time-dependent) fraction of the shallow convective contribution (see below) which is supposed to approximately balance the boundary-layer heat and moisture fluxes. The closure might also be interpreted as providing a correction to the prediction of convective ensemble properties (mass flux) by simple parcel theory (CAPE). Importantly, the different factors in (16) mutually interact, and it will be shown that when integrated over a diurnal cycle (16) roughly produces the same daily averaged mass flux and precipitation as (11). The scaling (17) is consistent with the free tropospheric and energy conversion scaling suggested in Shutts and Gray (1999), when using the surface buoyancy flux instead of the integrated tendencies. In the following the closure specified by (16) is referred to as NEW.

2.3 Closure for shallow convection

A distinction between deep and shallow convection is made on the basis of the first-guess convective cloud depth. If the cloud extends over more than 200 hPa then convection is classified as deep, and shallow otherwise. This distinction is only necessary for the closure and the specification of the entrainment rates that are a factor of two larger for shallow convection (see Appendix). In the case of very shallow convection both PCAPE and the denominator in (16) tend to zero, and a closure based solely on boundary-layer equilibrium becomes appropriate. A closure for shallow convection is obtained by assuming a balance between the second and third term of the rhs of (4), (i.e. a balance between the convection and the mean advection and other physical processes in the boundary-layer), and replacing

the tendency for PCAPE by the vertically integrated tendency of the moist static energy h

$$\int_{p_{\rm surf}}^{p_{\rm base}} \left.\frac{\partial \bar{h}}{\partial t}\right|_{\rm CONV} dp = g\left|_{p_{\rm surf}}^{p_{\rm base}} F_h = -\int_{p_{\rm surf}}^{p_{\rm base}} \left.\frac{\partial \bar{h}}{\partial t}\right|_{\rm BL} dp, \right. \tag{18}$$

where F_h is the convective moist static energy flux. Assuming zero convective mass flux at the surface, the cloud base mass flux is then obtained as

$$M_{\rm base}\left[h^{\rm up}_{\rm base} - \bar{h}_{\rm base}\right] = -\frac{1}{g}\int_{p_{\rm surf}}^{p_{\rm base}} \left.\frac{\partial \bar{h}}{\partial t}\right|_{\rm BL} dp; \quad M_{\rm base} \geq 0. \tag{19}$$

The deep and shallow convective closures (11), (16) and (19) together with the entrainment/detrainment rates (A.1)-(A.3) take into account the vertical stratification and/or the boundary-layer tendencies. Together with the horizontally variable time-scales $\tau_{\rm c}$, and $\tau_{\rm bl}$, the closures provide a flexible framework so that the convective fluxes can adjust to varying synoptic and boundary conditions.

3 Diurnal cycle of precipitation

3.1 Climatology

The diurnal cycle of convection in the IFS is first evaluated from an ensemble of one-year integrations and compared against a 10-year precipitation climatology from TRMM (Nesbitt and Zipser, 2003; Takayabu and Kimoto, 2008). The simulations are forced by analysed sea surface temperatures, and use spectral truncation n=159 (Δx=125 km) with 91 vertical levels, and a time step of 1 hour. Precipitation data from both the simulations and the observations are composited in hourly bins, and the diurnal amplitude and phase are computed from the first harmonic of a Fourier series.

The diurnal amplitude (mm day^{-1}) of the precipitation in the tropical belt from the TRMM radiometer is displayed in Fig. 1a. Maximum amplitudes reach around 10 mm day^{-1} over tropical land. Amplitudes from the model integrations using the CTL and NEW closures are displayed in Figs. 1b-c. Overall, the spatial distribution of the amplitudes is reasonably reproduced in the simulations, but the simulated amplitudes reach higher values, particularly over northern Amazonia. However, the simulated total rainfall over Amazonia appears realistic when compared to the GPCP2.2 dataset (not shown).

The corresponding phase of the diurnal cycle (LST) is displayed in Fig. 2. As already discussed in earlier studies, maximum precipitation in the TRMM radar data (Fig. 2a) occurs over tropical land roughly in the late afternoon to early evening, though strong regional variations are present. In particular, in the TRMM climatology convective rainfall over Amazonia occurs during the early afternoon, but may peak as early as local noon due to the high relative humidity and low stability in the lower troposphere (Betts and Jakob, 2002). In contrast, maximum precipitation over the tropical oceans occurs during the early morning. The CTL (Fig. 2b) provides a reasonable reproduction of the diurnal phase over water, but the convective precipitation over land generally peaks around local noon, except over Amazonia where it peaks during late morning. This systematic model error has not improved significantly in the IFS over the last decades (Slingo et al., 1992; Bechtold et al., 2004). However, a marked improvement is obtained with the NEW closure that shifts the diurnal cycle over land by 4–5 hours compared to CTL, and also improves the diurnal cycle in coastal regions, (e.g. off the Central American and West African coasts, as well as off the Indian subcontinent, and over the Maritime Continent). Experimentation shows

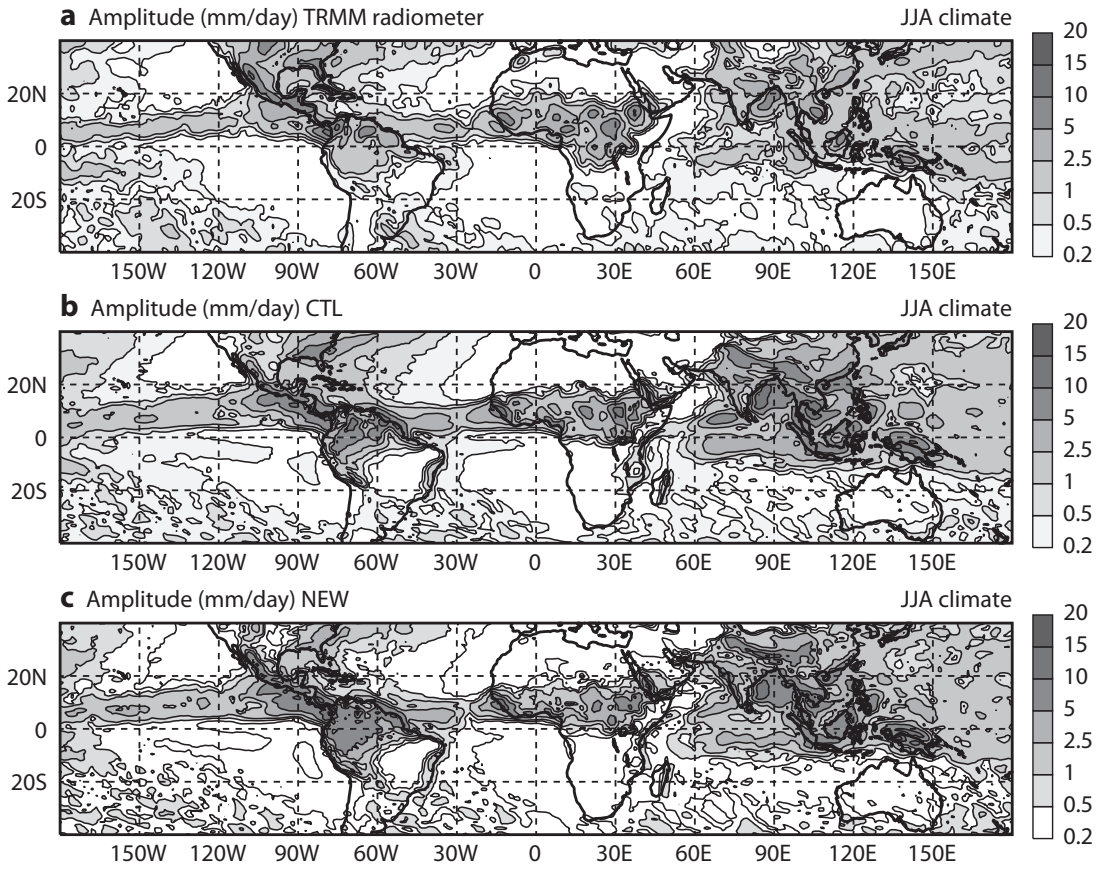

Figure 1: Diurnal amplitude (mm day^{-1}) of the precipitation in the tropical band as obtained (a) from a 10-year climatology of TRMM radiometer data (courtesy Yukari Takayabu and colleagues), and from an ensemble of annual IFS integrations at truncation n=159 (Δx =125 km) with (b) the CTL, and (c) NEW closure.

that the improvements over coastal regions are primarily due to a better representation of the convection generated over land and advected over sea, along with the associated subsiding motions, but the modified adjustment over sea via τ_{bl} also contributes.

3.2 High-resolution integrations

In addition to seasonal integrations, higher resolution daily 3-day forecasts have been performed for June, July and August (JJA) 2011 and 2012 using n=511 ($\Delta x = 40$ km) with 137 vertical levels and a time step of 900 s. The forecasts were initialised from ECMWF's operational analyses at n=1279 ($\Delta x = 16$ km) with 91 levels. The forecasts are compared to the NCEP Stage IV composites (Lin and Mitchell, 2005) obtained from the combination of radar and rain gauge data (NEXRAD, hereafter) over the continental United States during summer 2011 and 2012, and German radar composites from the Deutsche Wetterdienst for summer 2011. All forecast days have been used to compute the diurnal composites that is 3×90 days for each JJA season.

The amplitude and phase of the diurnal cycle of precipitation averaged over the summers 2011 and 2012 are depicted in Fig. 3 and Fig. 4 for the continental United States. Numerous previous studies have already described the diurnal cycle over this region (e.g. Dai et al., 1999; Tian et al., 2005). In summary,

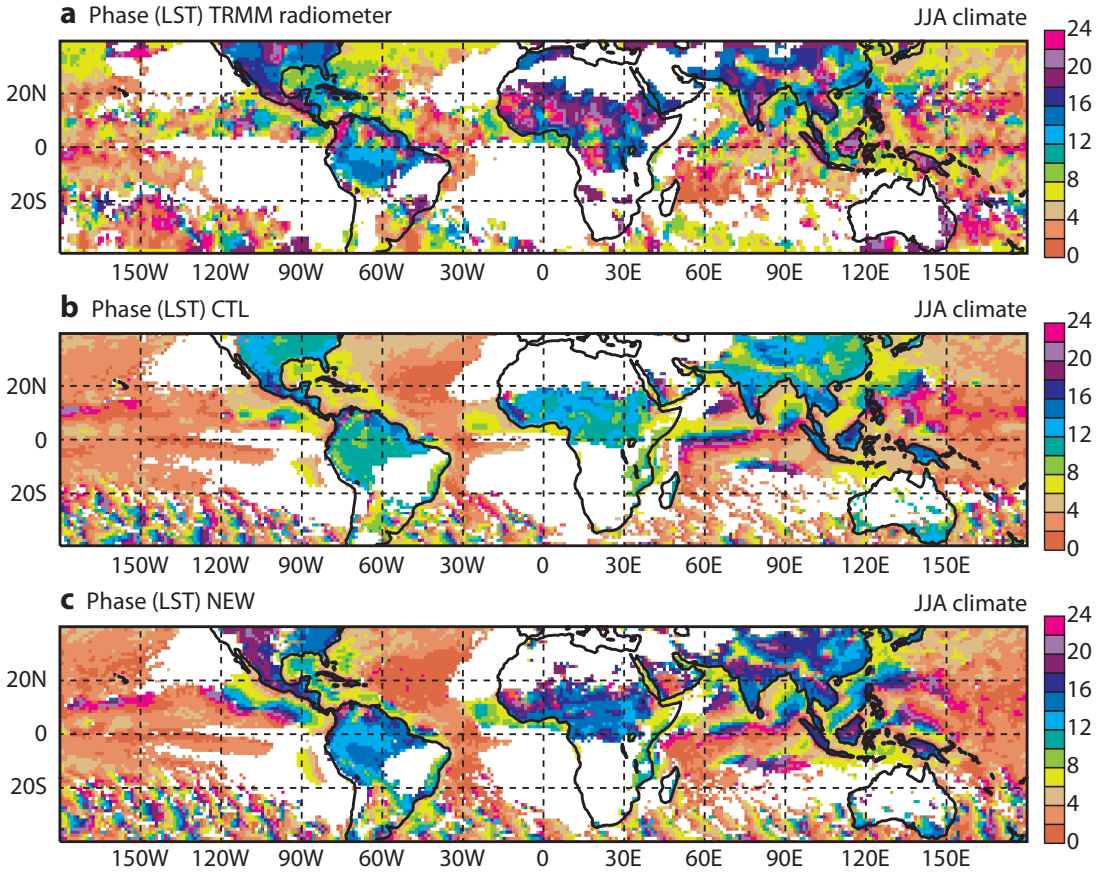

Figure 2: Same as Fig. 1, but for the diurnal phase (LST) of the precipitation. Also, TRMM radar data has been used instead of the radiometer data. White shading is applied for areas where the amplitude of precipitation is below 0.2 mm day^{-1}.

as is also evident from the NEXRAD data (Fig. 3a and Fig. 4a), the diurnal cycle over the continental United States is characterized by three distinctive regions, the Rocky Mountain area, where convective activity peaks during the late afternoon, the Central Plains with predominantly nighttime convection from propagating mesoscale convective systems triggered over the Rocky Mountains, and finally the Eastern United States and coastal regions with predominantly late afternoon convection and a particularly strong diurnal amplitude over the Florida peninsula.

The CTL forecasts have quite a reasonable representation of the spatial variations in the amplitude (Fig. 3b), but underestimate the amplitude east of the mountain ridge and somewhat overestimate the amplitude in the coastal regions. The results with the NEW forecasts are rather similar though slightly improve on the CTL. However, concerning the phase (Fig. 4) the NEW forecasts substantially delay the diurnal cycle by 4–5 hours compared to CTL so that the results more closely match the observations, though over the Eastern United States the diurnal cycle in NEW still precedes the observed cycle by up to 2 hours.

To give an overview of the diurnal cycle in the high-resolution short-range forecasts, the area-averaged diurnal rainfall composites are depicted in Fig. 5 for the Eastern United States and Germany and also for the central Sahel region, which has TRMM climatological data for comparison. The area-averaged representation shows that NEW has quite a good fit to the daytime and evening diurnal cycle of precipitation, shifting it by up to 6 hours compared to CTL. The late night precipitation, however, remains

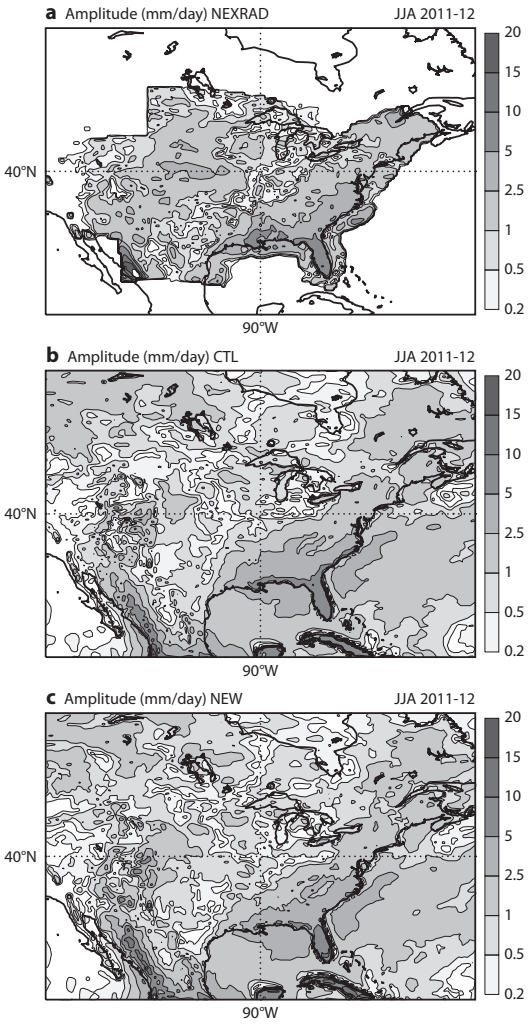

Figure 3: Amplitude (mm day^{-1}) of the precipitation averaged over JJA 2011 and 2012 for the continental United States from (a) NEXRAD, and from daily 72-hour forecasts at truncation n=511 (Δx =40 km) with (b) CTL and (c) NEW closure. The RMSE against observations does not differ significantly between CTL and NEW.

underestimated in both NEW and CTL in spite of having the convection parametrization coupled to a five-species prognostic cloud scheme via the detrainment of convective condensate. The late-night precipitation deficit might be due to the missing representation of convective system dynamics including spreading surface cold pools and predominantly upper-level mesoscale lifting during the night. Finally, over the Sahel (Fig. 5c), NEW realistically increases the precipitation with respect to CTL. As shown by Marsham et al. (2013), a correct phase representation of the diurnal cycle is particularly important in this region where the convective heating is a key driver of the meridional pressure gradient and the large-scale dynamics.

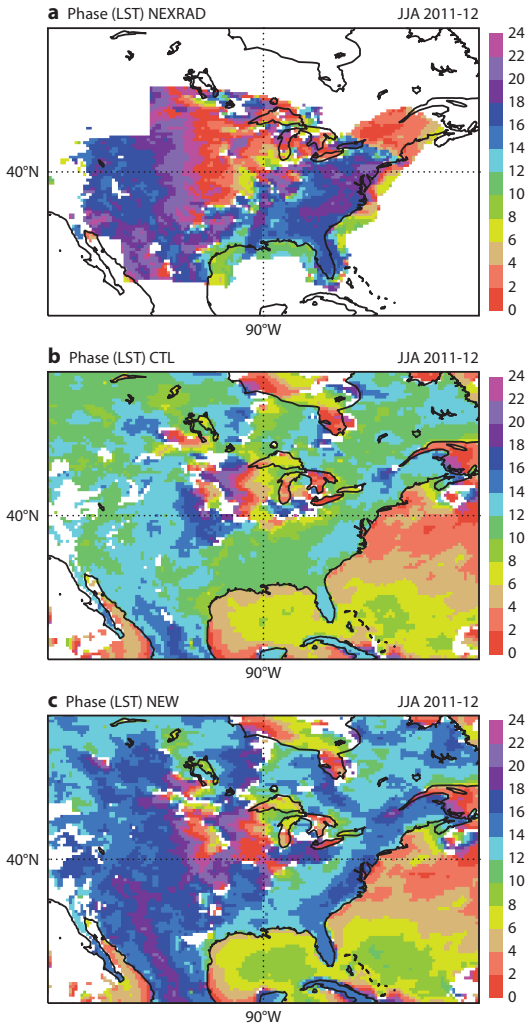

Figure 4: Same as for Fig. 3, but for the diurnal phase of the precipitation (LST).

4 Discussion

In the following we focus on the central Sahel region (as defined in Fig. 5c) for the analysis of the convective closure, and also provide further evaluation of the convective heating and its dynamical response using CRM and complementary satellite data. All model results are based on the high-resolution short-range forecasts discussed in the previous section. In addition to the forecasts, data assimilation cycles have been run with the IFS, providing a more direct comparison of model and data in space and time. The CRM data is from the Meso-NH limited area model (Lafore et al., 1998) that has been run during 10–25 June 2012 at 2.5 km grid-spacing daily for 24-hours over the central Sahel region defined in Fig. 5c (i.e. roughly a 2200 by 1700 km large domain). The CRM uses the same ECMWF n=1279 analyses as initial conditions as are used for CTL and NEW. In addition, the CRM open boundaries are updated every 6 hours from the analyses.

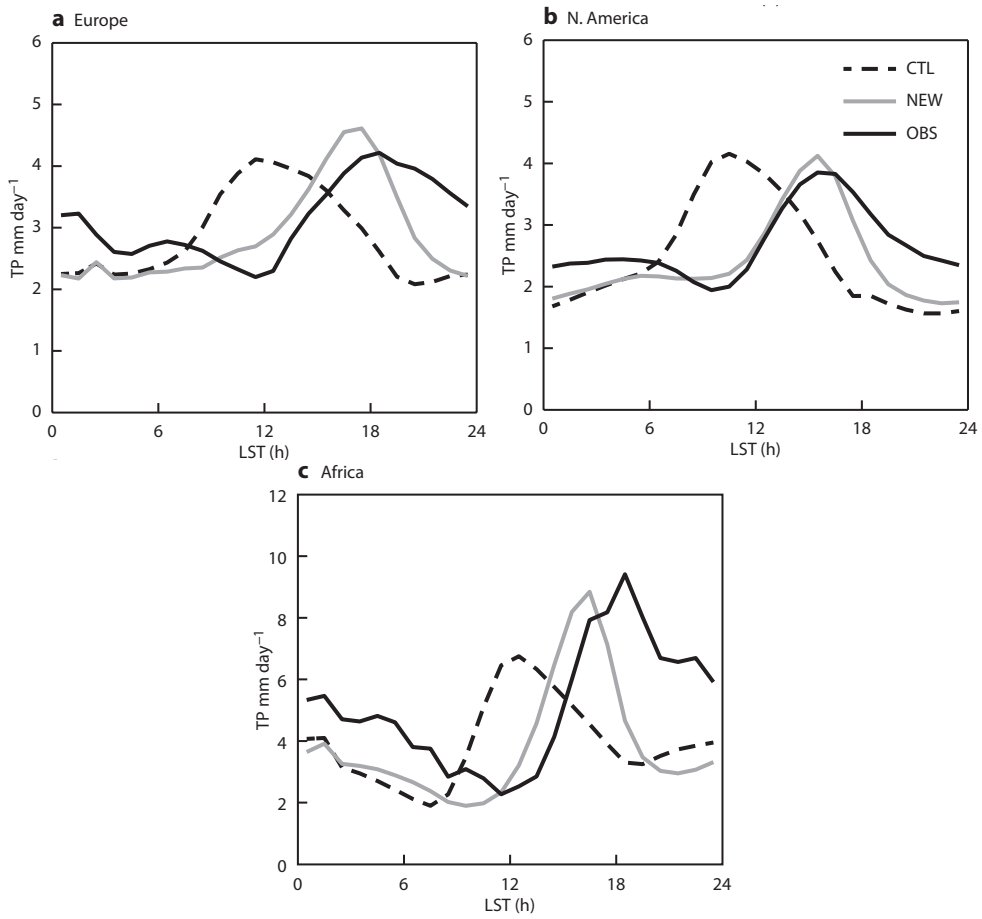

Figure 5: Diurnal composites of area averaged total precipitation (mm day^{-1}) from CTL (black solid lines), and NEW (dashed lines) against observations for JJA 2011 (Europe) and JJA 2011 and 2012 for the other areas: (a) Germany [48°–52°N,7°–14°E] using DWD radar, (b) eastern United States [30°–45°N,100°–80°W] using NEXRAD, and (c) central Sahel region [5°–20°N,10°–30°E] using TRMM climatological radiometer data.

4.1 Diagnostics on closure

Diurnal composites of quantities related to the convective closure are illustrated in Fig. 6 for the period 10–25 June 2012; shown are the total-area averages (dashed lines) and averages only over the convectively active grid columns (solid lines) which are also labeled by the suffix c (convective). The quantities considered in Fig. 6 include the surface convective precipitation rate, the CAPE (1), and the various terms involved in the closures (11) and (16): (a) the cloud-base convective mass flux, (b) PCAPE$'$ that takes value PCAPE in CTL, and value PCAPE-PCAPE$_{\rm bl}$ in NEW, (c) the convective adjustment time-scale τ (12) and (d) the stabilization by compensating subsidence (7). The surface convective precipitation rate is proportional to the convective mass flux at cloud base times the updraught rain/snow content, though over land it is also strongly affected by evaporation in the subcloud layer. It is also approximately equal to the total surface precipitation as most stratiform precipitation evaporates before reaching the ground.

Concerning the total area averages, one notices that for both, CTL and NEW the convective precipitation, mass flux and PCAPE$'$ are in phase. The forecasts barely differ during night, but there is a clear 5 hours shift in the maxima in NEW with respect to CTL. CAPE (Fig. 6b) has been computed diagnostically for

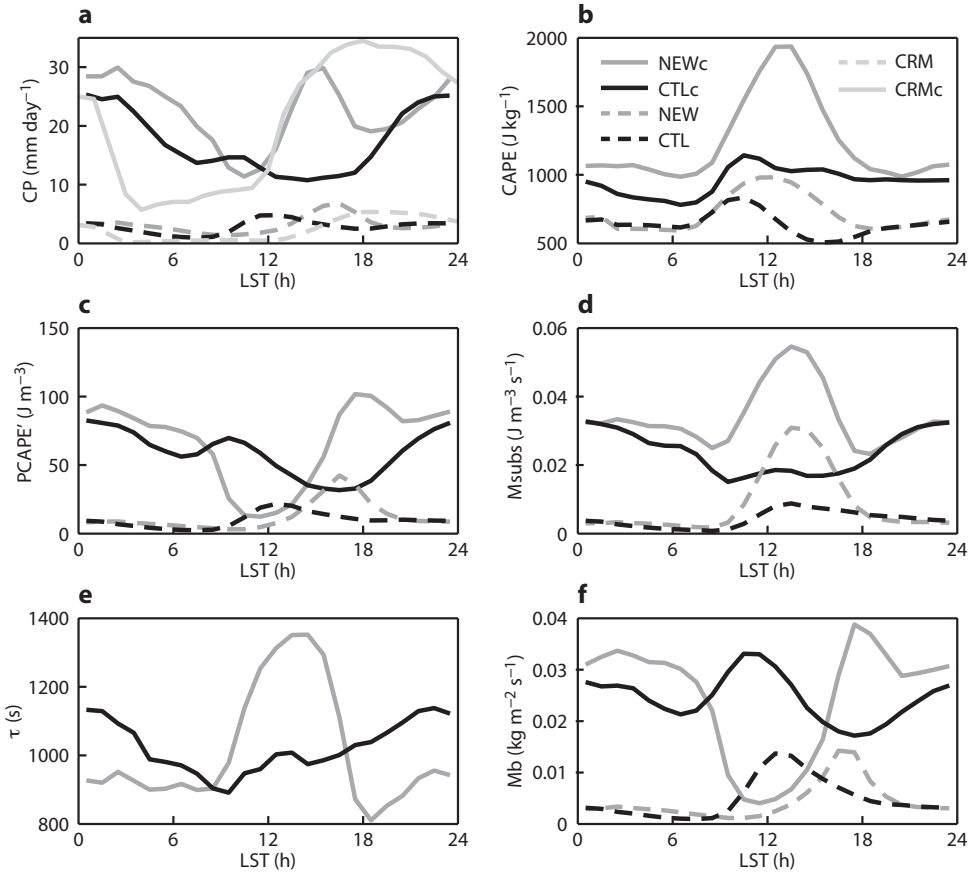

Figure 6: Diurnal composites of convective closure related diagnostics during 10-25 June 2012 over the central Sahel region: (a) Convective precipitation, (b) CAPE, (c) PCAPE′=PCAPE for CTL and PCAPE-PCAPE$_{bl}$ for NEW, (d) the compensating mass flux term (5), (e) the convective adjustment time scale τ, and (f) the cloud base mass flux. Dashed lines denote total area averages and solid lines and legends with suffix c denote averages over the regions with convective precipitation. Precipitation statistics from the CRM are included in (a), with the precipitation rates per rain event scaled accounting for the difference in resolution between the CRM and the IFS.

all grid columns from the mean thermodynamic profiles, while PCAPE is computed inside the convection scheme and therefore is non-zero only in grid-columns with active convection. CAPE has much larger values than PCAPE, reflecting the importance of entrainment. The main conclusion here is that CAPE shows an unphysical maximum at 10 LST in CTL, if taken as either a domain average or averaged over the convective regions, while its evolution in NEW roughly follows the evolution of the surface heat fluxes.

The evolution of the convective area averages CTLc, NEWc and CRMc (solid lines) is more revealing. Note that the cloud base mass flux (or convective precipitation) is proportional to PCAPE$'/\tau$ divided by the subsidence term. In CTLc most closure related quantities peak around 10 LST, vary only weakly during daytime, and precede the peak in domain mean mass flux and precipitation by about 2 hours. In contrast, the daytime amplitudes are important in NEWc, and the total domain and convective domain averages are in phase. It will be shown later that the reason for this is that the convection in NEW is strongest at the end of the lower tropospheric moistening phase, while in CTL the convection is already active during the strong moistening phase. Interestingly, the convective precipitation rate per event (solid lines in Fig. 6a) is minimum during the day in CTLc, while NEWc produces precipitation rates per event

that peak at around 30 mm day^{-1} during late afternoon which is more in line with the observed rain rates from mesoscale convective systems in the Sahel (Mathon et al., 2003). For comparison we have also plotted in Fig. 6a the total-area mean (dashed grey line), and resolution-scaled rainy area mean precipitation (solid grey line) from the CRM, though data on the diurnal cycle from CRM also has to be interpreted with care (Langhans et al., 2012). The evolution of the total-area mean precipitation in the CRM during daytime is comparable to that of NEW, but peaks 1–2 hours later. Responsible for this shift is the growth in number and size of convective systems in the CRM during late afternoon and their tendency to produce more surface precipitation through reduced evaporation; these features are more difficult to represent with a diagnostic convection formulation. The CRM also produces more precipitation during the night which is consistent with radar observations (Fig. 5). Interestingly, the onset of convection around 12 LST, average intensity and its evolution during the afternoon (as measured by the rainy area mean precipitation) compares reasonably well between NEW and the CRM. The low early morning rain rates in the CRM are related to boundary-layer spin-up processes (discussed later).

The low total-area mean precipitation rates in NEW in the late morning and early afternoon are the consequence of low values of PCAPE′ in connection with long adjustment times and moderate subsidence stabilization (Figs. 6a,c-e). It will be illustrated in the next section that the resulting convective heating keeps the free troposphere in a marginal stability regime. The increase in the convective adjustment time during late morning is produced by an increase in the cloud depth, while its decrease in the afternoon is caused by an increase in the mean updraft velocities. In conclusion, in non-stationary or non-equilibrium convection the various contributors to the forcing and stabilization interactively adjust. A successful simulation of the diurnal cycle requires most importantly a realistic formulation of the evolution of PCAPE′ which is dependent on the entrainment rates. The adjustment time-scale (12), which depends on PCAPE, is also an important factor for the representation of the spatial and temporal variability of convection.

4.2 Heating and moistening profiles

Composite diurnal cycles of the vertical distribution of the total heating rate (but excluding the radiative heating), and the total moistening rate, are illustrated in Fig. 7. Using units of K day^{-1}, these quantities are usually referred to as $Q_1 - Q_{\text{rad}}$ and $-Q_2$, respectively. The heating and moistening rates due to adiabatic motions have also been added as contours in Fig. 7 in order to distinguish convective and dynamical forcings.

One recognizes for both CTL and NEW (Fig. 7a,c) a distinctive phase with deep boundary-layer heating from 6:30 to 12 LST, followed by boundary-layer cooling and more elevated dry and shallow convective heating lasting until 17 LST. Boundary-layer moistening lasts until roughly 9 LST, followed by strong drying of the lower boundary-layer, and dry and shallow convective moistening of the lower troposphere extending to or exceeding the 600 hPa level at 15–16 LST. In both CTL and NEW, during the afternoon, there is also a strong drying by mean advection around 850 hPa that has also been noticed in observational studies (Zhang and Klein, 2013). During the strong growth phase of the boundary-layer from 10–17 LST, corresponding to a continuous growth of PCAPE′ in NEW (Fig. 6), the heating in the upper part of the boundary-layer is in balance with the cooling due to adiabatic motions, but the upper-troposphere is not in equilibrium. Indeed, the evolution of the upper-tropospheric heating profiles differs strongly between CTL and NEW. Whereas in CTL the mid- to upper-tropospheric heating of 5–10 K day^{-1} from precipitating deep convection occurs around 13 LST, and therefore during the growth of the boundary-layer, the strong deep convective heating in NEW occurs when the lower- to middle-troposphere has reached its maximum total heat content. Note that in NEW modest mid-tropospheric heating and therefore stabilization occurs from around 11 LST onwards, and is due to cumulus congestus reaching heights of 500-400

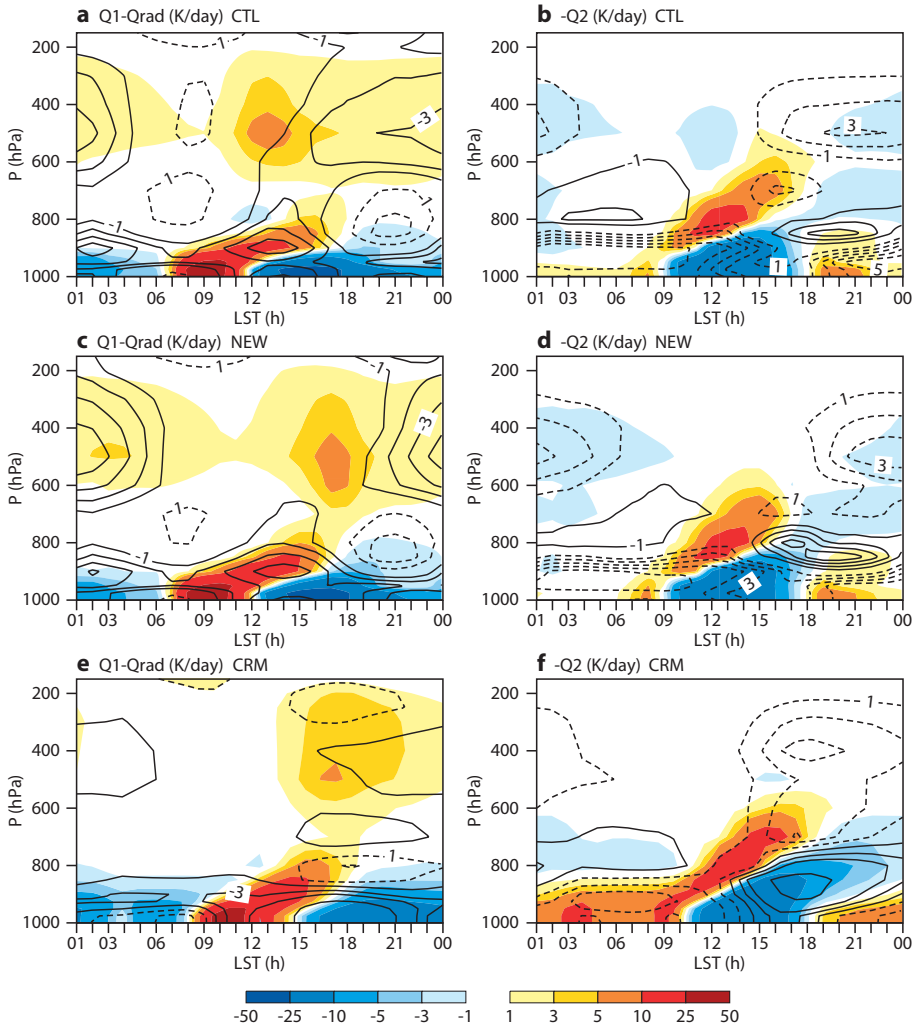

Figure 7: Diurnal composites of heating and moistening rates (K day^{-1}) during 10-25 June 2012 over the central Sahel for (a) and (b) CTL, (c) and (d) NEW, and (e) and (f) from the CRM. Total heating rates minus radiation, $Q_1 - Q_{\mathrm{rad}}$, and total moistening rates $-Q_2$ are shaded. Solid contour lines denote cooling and drying rates due to adiabatic motions, dashed contour lines (interval 1 K day^{-1}) denote adiabatic heating and moistening.

hPa.

The dynamic response to deep convective heating is a couplet of upper-tropospheric cooling (lifting) and lower-tropospheric warming (subsidence) often called the stratiform mode. Through the quasi-geostrophic adjustment process it becomes effective a few hours after the convective heating. This dynamic cooling/heating couplet is particularly important for the formation of mesocale stratiform rain during night. The upper-tropospheric response in NEW is clearly delayed, and is stronger than in CTL, attaining values of -4 K day^{-1} . Nevertheless, NEW still underestimates the nighttime precipitation with respect to the observations (Fig. 5).

A comparison of the heating and moistening profiles with CRM data (Fig. 7e,f) reveals that NEW produces a realistic diurnal cycle in phase and amplitude, including the shallow and congestus heating phase, though the latter is less pronounced in the CRM. The heating profiles Fig. 7c,e are also in fair agreement with the observed cloud evolution during days with late afternoon convection as reported by

Zhang and Klein (2010). Interestingly both in NEW and the CRM the maximum upper-tropospheric heating of up to 10 K day^{-1} occurs around 17 LST. However, the heating peaks at higher altitudes in the CRM (400 hPa compared to 500 hPa in NEW), extends over a larger depth, and maintains its amplitude during the early night hours as does the surface precipitation. The moistening rates -Q2 (Fig. 7d,f) are also in good agreement during daytime. However, larger differences in the heating profiles between the CRM and the IFS exist in the early morning hours which can be partly attributed to boundary-layer spinup processes in the CRM.

The dynamic response to the convective heating is also comparable in structure and intensity between the CRM and NEW. The main difference is that the dynamical cooling is somewhat weaker in the CRM, but occurs earlier; i.e. shortly after the maximum heating. The phase lag in the dynamical response between NEW and CRM becomes even more evident for the moistening profile (Fig. 7f). The reason for this phase difference is a tight coupling between resolved microphysics (condensation) and resolved dynamics (lifting) in the CRM, whereas with parametrized convection (a) the heating rates Q1 and Q2 already contain a contribution from subgrid transport, and (b) the resolved flow has to adjust in response to a subgrid heat source. Furthermore, the dynamical drying in the CRM extends down to the surface between 15 and 18 LST when also strong dynamical cooling occurs. This dynamical feature is a signature of resolved downdrafts and cold pools in the CRM. Generally, we think that the structure and evolution of the convective heating and its dynamical response compares fairly between the CRM and NEW, given the limited domain size of the CRM and its sensitivity to the parametrization of horizontal mixing.

4.3 Clouds and heating against satellite observations

To further assess the structure and temporal evolution of the convective heating, the IFS has also been run in 4D-Var data assimilation mode, permitting a better temporal and spatial evaluation against satellite data from geostationary infrared imagers and sun-synchronous microwave profilers.

A composite diurnal cycle of infrared brightness temperatures (BTs) in the 10.8 μm window has been computed in Fig.8; it is representative for the Sahel for June to July 2012. The composites have been derived from two-dimensional probability density functions (PDFs) of BTs of the observed 1-hourly Meteosat 9 images, and the BTs from synthetic satellite images from day-2 forecasts using the CTL and NEW, all data has been interpolated to a 0.4° grid. The observed BTs vary between 325 and 180 K, while the minima in the forecasts remain above 190 K. The forecast synthetic BTs have been bias corrected by -3K, but there is still an important bias during the night corresponding to an underestimation of optically thick high clouds and nighttime precipitation as already seen in Fig. 5. However, during the day the mean BTs from NEW closely follow the observed diurnal cycle, though the variability is still underestimated. In contrast, in the CTL, due to the occurrence of deep convection being too early, the BTs are too cold during noon and early afternoon, and too warm in the evening, where the variability is also strongly underestimated. The improved variability in NEW, and indeed better spatial representation of convection compared to CTL (not shown), is a consequence of the higher CAPE values and more realistic adjustment of the free troposphere. The interpretation of the improvement (cooler BTs) of NEW compared to CTL during the early morning hours is less obvious. Further investigation shows that this is caused by a combination of lower skin temperatures due to increased precipitation and soil moisture in the northern part of the domain, more residual elevated clouds from nighttime convection, and a more realistic convection in the tropical convergence zone extending into the southern part of the domain. All together, the results in Fig. 8 are consistent with the comparison against radar data given in Fig. 5.

Finally, a global picture of the improvement in the heating structure of NEW compared to CTL is given in Fig. 9 using July 2012 as an illustration. This shows a reduction in root-mean-square (rms) error of

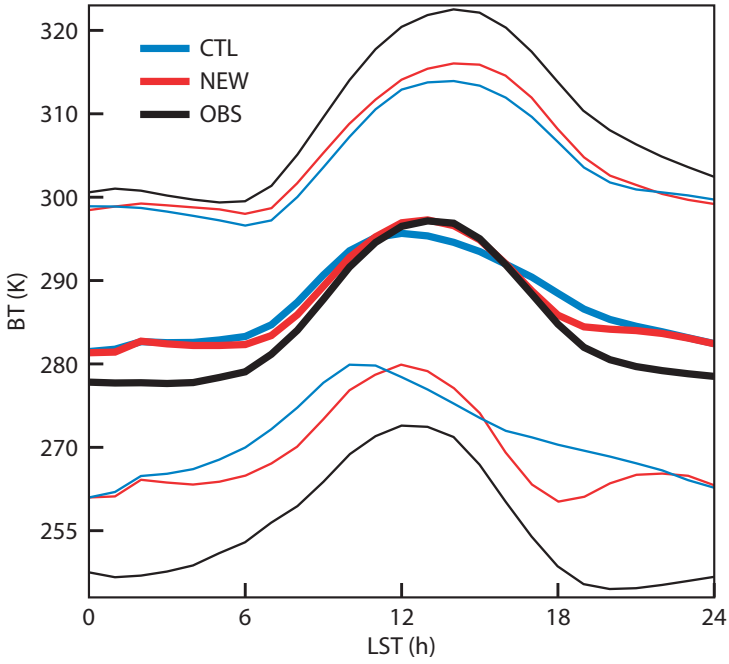

Figure 8: Diurnal composite of mean and standard deviation of infrared BTs (K) in the 10.8µm window during June to July 2012 over the central Sahel from Meteosat 9, and from the day-2 CTL, and NEW forecasts. The composites have been computed from a two-dimensional PDF, and a -3K bias correction has been applied to the forecasts. Thick lines correspond to median values, and thin lines to ± one standard deviation.

the BTs when evaluating the short-range (first guess) forecasts during the 12-hour assimilation window against the clear-sky BTs from AMSU-A microwave sounders on-board sun-synchronous NOAA satellites. The satellites have different twice-daily overpass times, and the results are shown for two channels, sensitive to temperature over broad atmospheric layers around 500–1000 and 250–600 hPa. Clearly, NEW provides an improvement over CTL over most land regions with persistent active convection, and in particular in the middle to upper-troposphere where the convective heating is strongest. The improvement of order 0.1 K is primarily a result of a reduction in the bias for the day-time overpasses. It is small in absolute values, but it is statistically significant, and has to be compared to the absolute rms error of the 12-hour forecasts that does not exceed 0.3 K. The areas of reduction in the short-range forecast errors are consistent with the improvements in the diurnal cycle seen in the long integrations (Fig. 2).

5 Conclusions

An entraining CAPE-dependent diagnostic closure for the cloud base mass flux has been derived under the assumption of free tropospheric quasi-equilibrium that is subject to boundary-layer forcing. The closure involves a convective adjustment time-scale τ for the free troposphere that is proportional to the convective turnover time-scale, and a coupling coefficient between the boundary-layer and the free troposphere based on different time-scales over land and water. With this formulation, only at the end of the lower tropospheric heating and moistening cycle is the entire CAPE available to the convection.

The part of CAPE generation by boundary-layer heating that is not available for consumption by deep convection motions is roughly proportional to the ratio α times the surface heat fluxes. Typical values

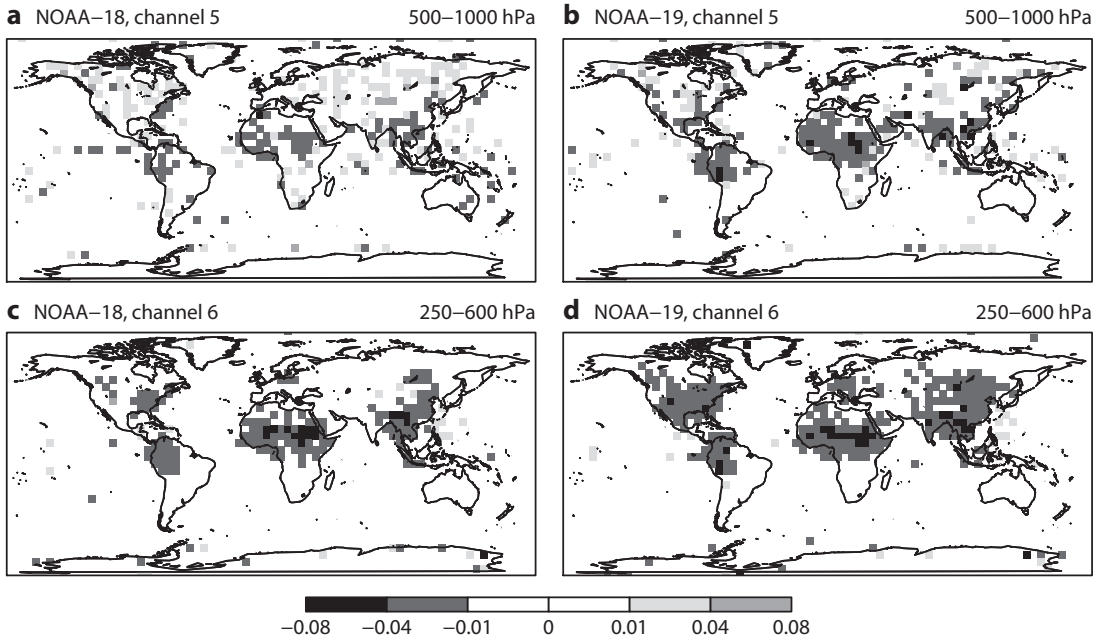

Figure 9: Root mean square error differences in clear-sky BTs (K) for July 2012 between NEW and CTL during the 12-hour window of the 4D-Var analysis, when evaluated against AMSU-A microwave sounding channels on-board NOAA sun-synchronous satellites. The channels are representative for different atmospheric layers: (a) and (b) NOAA-18 and 19 channel 5 for the 500-1000 hPa layer, and (c) and (d) NOAA-18 and 19 channel 6 for the 250-600 hPa layer. The twice daily overpass times are 03 LST and 15 LST for NOAA-18, and 01:30 LST and 13:30 LST for NOAA-19.

of $0 \leq \alpha < 0.1$ reproduce the current model version CTL, which produces a diurnal cycle of convection over land that peaks around local noon. The NEW closure uses values of α over land in the range of $0.5 < \alpha \leq 1$. It is a pragmatic approach based on simple scaling arguments. This closure might numerically account for the gap between parcel theory (CAPE) and ensemble mean property (mass flux), but equivalent numerical results might in principle also be obtained with the aid of a (prognostic) plume ensemble. We do not yet know if this closure and the parameter range for α indeed reflects the actual physical coupling between the boundary-layer and the deep convection, e.g. by implicitly accounting for the CIN/activation control where a shallow near-surface heating maximizes the effect on CIN, whereas a deep tropospheric anomaly maximizes the effect on CAPE (Mapes, 2000; Parker, 2002). It would be interesting to perform, in the parametrization context, further analyses of the coupling between the boundary-layer and the deep convection based on observations and data from CRM. But this clearly is beyond our scope.

It has been shown through comparison with complementary data sources (e.g. radar data, and satellite data from infrared imager and microwave sounders) that NEW provides a fair representation of the observed daytime evolution of convection over land, and increases its variability and intensity due to larger CAPE values in the afternoon. Furthermore, in NEW the shallow and congestus convection is present during the morning and early afternoon, respectively, while intense deep convection only sets in near the end of the lower to mid-tropospheric heating and moistening cycle. This is in agreement with CRM data. The results are essentially independent of model resolution and time step. However, the current diagnostic formulation of convection with its diagnostic rain production is a limitation. We think that a further shift of the maximum precipitation by 1–2 hours might be obtained by (a) coupling the

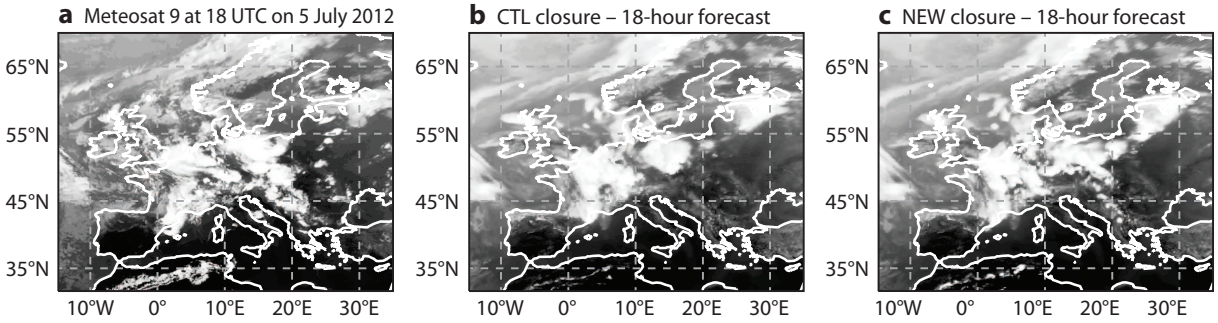

Figure 10: Infrared 10.8 μm satellite image over Europe on 5 June 2012 18 UTC from (a) Meteosat 9 channel 9, and from the 18-hour forecasts at n=1279 ($\Delta x = 16$ km) with (b) CTL, and (c) NEW. All images are at resolution 0.2°.

convection to the stratiform prognostic microphysics not only via the condensate detrainment term, but also via precipitating species, or (b) by using a more prognostic formulation of the convection.

A full verification and discussion of the impact of NEW on the general model performance is beyond the scope of the paper. As an illustrative example, Fig. 10 shows at resolution 0.2° the observed 10.8μm infrared satellite image over Europe on 1 July 2012 and the synthetic forecast images from the n=1279 (Δx=16 km) 18-hour forecasts. Indeed, NEW better represents the mainly surface-driven convection over the Balkans and the Atlas mountains, a situation that can be frequently observed during summer. But compared to CTL it also improves for the strongly synoptically-forced convection over central Europe, where the timing of convection matters for the evolution of the mesoscale weather patterns. Further verification (not shown) confirms that the overall model performance, including the fit to wind data from soundings and profilers is improved over the tropical land regions and the middle latitudes during summer. Notably, at 18 LST near surface temperatures are increased by 0.2–0.5 K, and boundary-layer wind turning is increased. NEW is planned to become the operational version of the IFS in autumn 2013.

So far, there has been little discussion on the effect of NEW over the oceans. In these areas, the overall synoptic impact can be described as largely neutral, including the medium-range forecasts of tropical cyclones and the representation of the Madden-Julian oscillation in seasonal integrations. However, there is a positive impact on the representation of convection and the diurnal cycle in near-coastal areas. Of particular concern in NWP is, for example, the inland advection of wintry showers forming over the relatively warm sea. This is illustrated by Fig. 11 which shows the 24-hour precipitation accumulations over the British Isles and the near European mainland on 1 December 2010 as observed from ground-based radar along with the 24-hour forecasts for CTL and NEW with n=1279. Nearly all precipitation accumulated as snow on the ground, reached up to 20 cm and was predominantly of the convective type. Clearly, NEW reduces the unrealistically strong snowfall along the coast by up to 50% compared to CTL, and more realistically moves the convective snowfall inland, bringing up an extra of 10 cm snow (Fig. 11d). This is possible even with a diagnostic formulation of convection as the moist unstable air is advected inland, and the simulated convection is formulated so that it is allowed to depart from elevated layers. The main difference between NEW and CTL is the slower convective adjustment, avoiding a too strong large-scale response leading to coastal convergence. An improved version of CTL for this particular case could also be obtained by increasing the convective adjustment time. However, tests showed that this would significantly degrade the general model performance, highlighting again the need for a more flexible and dynamically-targeted formulation of the convective adjustment in NWP.

Finally, concerning future higher-resolution upgrades of the IFS, from the current n=1279 (16 km) oper-

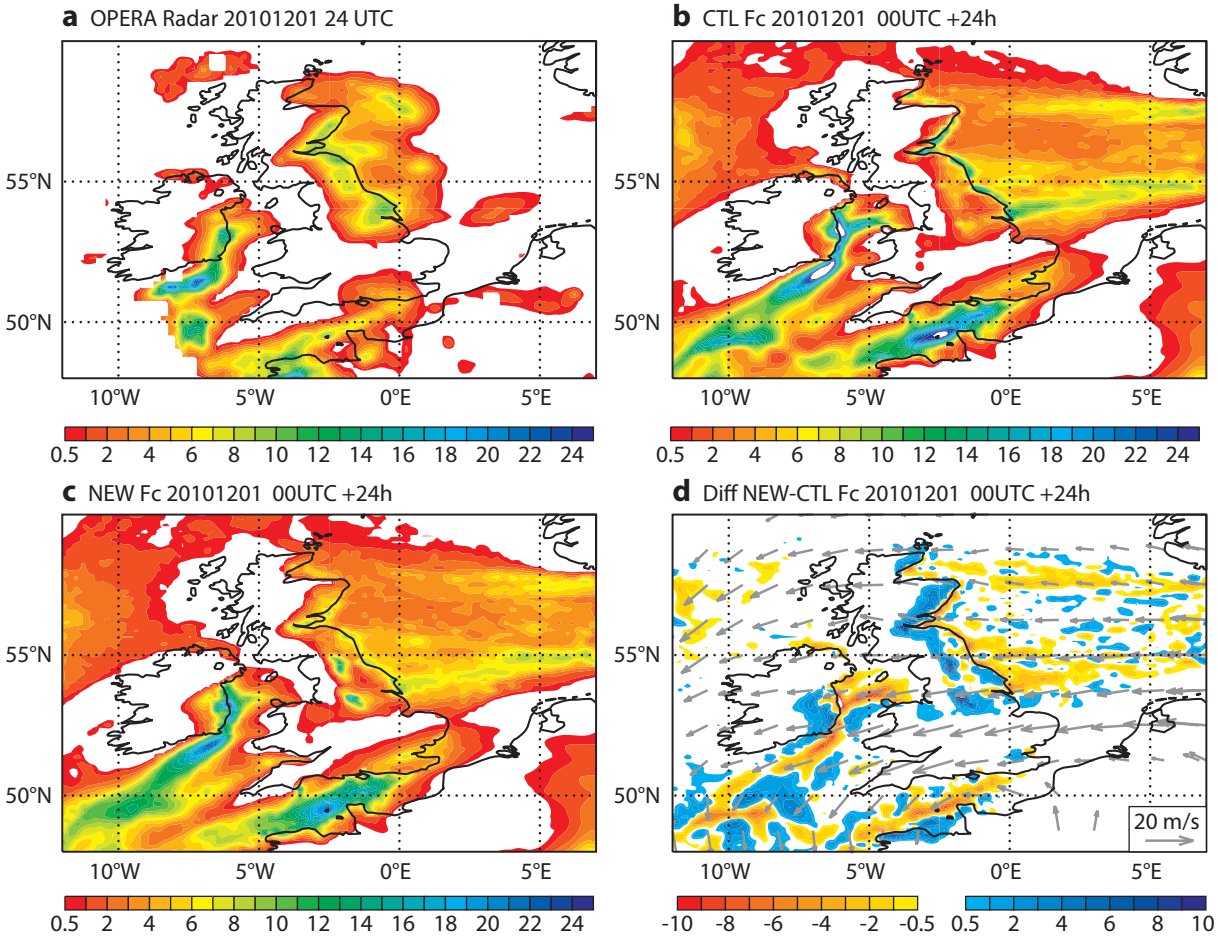

Figure 11: 24-hour precipitation accumulations (mm) for 1 December 2010 over the British Isles and near European mainland from (a) Radar observations on a 0.25° grid, and 24-hour n=1279 ($\Delta x = 16$ km) forecasts with (b) CTL, (c) NEW, and (d) difference between NEW and CTL. The advection is represented in (d) by the mean 500-850 hPa wind. NEW improves the RMSE against observations by 2% compared to CTL.

ational resolution to the planned n=3999 (5 km) resolution in 2020, we think that the convective closure described here will enable a smooth transition from parametrized to resolved deep convection as there is no longer a substantial discrepancy in the phase and location between parametrized and resolved convection. However, the intensity of the parametrized deep convection does not naturally diminish as resolution increases. For reasons of forecast performance, (i.e. stronger stabilization with increasing forcing), the current adjustment time scale τ in (12) converges to the convective turnover time-scale as resolution increases. One possible way of achieving vanishing parametrized tendencies for deep convection at high resolution is to increase the resolution dependent factor $f(n)$ in (12) to infinity from some resolution onward, say n=2000 (10 km). By doing so, the so called 'small area approximation' in the mass flux formulation is indirectly corrected for by a scaling, and the shape of the convective profiles is conserved. Instead, it might be necessary to recognize the limits of the so called 'small area approximation' more thoroughly, and replace the grid-mean values in the computation of CAPE or PCAPE (2) by the actual values in the environment.

Acknowledgments

The first author expresses his gratitude to Profs Julia Slingo, Erland Källén, and Alan Thorpe for encouragements to never give up on the diurnal cycle. Two anonymous reviewers provided very helpful suggestions. We are also very grateful to Prof Yukari Takayabu and her group at Tokyo University for providing the TRMM data, and to Dr. Peter Bauer for processing these data. Numerous discussions and critical evaluation of the model by our colleagues Drs Irina Sandu, Richard Forbes and Takuya Komori were extremely helpful, as was the assistance by Anabel Bowen in preparing the figures, and by Dr Bob Riddaway in improving the text. We are grateful to the National Centers for Environmental Prediction (NCEP) for producing and the Joint Office for Science Support/University Corporation for Atmospheric Research (JOSS/UCAR) for providing the Stage IV precipitation composites over the United States and thank Dr. Klaus Stephan from Deutsche Wetterdienst for providing the German radar precipitation composites. This work has also greatly benefited from the European Commission's COST action ES0905, and 7$^{\text{th}}$ Framework Programme EMBRACE project under Grant Agreement number 282672.

Entrainment and detrainment rates

A.1 Entrainment rates

Observations and CRMs show that mid-tropospheric relative humidity strongly controls the cloud top heights (e.g. Derbyshire et al., 2004; Zhang and Klein, 2010). A relative humidity (RH) dependent entrainment parametrization is used that has been shown to reasonably fit CRM data (de Rooy et al., 2013), and allows a realistic reproduction of the large-scale convectively coupled waves in the tropics (Bechtold et al., 2008; Hirons et al., 2013b). The fractional updraft entrainment rate E^{up} (m^{-1}) for deep convection is parametrized as

$$E^{\text{up}}_{\text{deep}} = \varepsilon^{\text{up}} \left(1.3 - RH\right) f_{\text{s}}, \quad \varepsilon^{\text{up}} = 1.8 \times 10^{-3} \text{m}^{-1}, \quad f_{\text{s}} = \left(\frac{q_{\text{sat}}(\bar{T})}{q_{\text{sat}}(T_{\text{base}})}\right)^3, \tag{A.1}$$

where q_{sat} is the saturation specific humidity.

Entrainment above cloud base is applied to positively buoyant convection only. For shallow convection the entrainment rates are increased by a factor of two, $E^{\text{up}}_{\text{shal}} = 2E^{\text{up}}_{\text{deep}}$, as also supported by CRM data. The vertical scaling function f_{s} in (A.1) is supposed to mimic the effects of a cloud ensemble and the effect of the cloud diameter increasing with height. As the scaling function strongly decreases with height, the updraft detrainment rate (see below) will eventually become larger than the entrainment rate, and the mass flux starts to decrease with height.

Turbulent entrainment rates for the downdrafts are set to a constant value of $3 \times 10^{-4} \text{m}^{-1}$. Downdraft organized entrainment is a function of buoyancy.

A.2 Detrainment rates

de Rooy et al. (2013) showed that detrainment rates can exhibit even larger variability than entrainment

rates. A careful specification of detrainment rates is necessary to correctly simulate the moisture and momentum budget near detraining regions such as the trade inversion and the tropopause.

Turbulent detrainment rates (m^{-1}) for deep convection are also assumed to be RH dependent

$$D^{\mathrm{up}}_{\mathrm{deep}} = \delta^{\mathrm{up}}\Big(1.6 - RH\Big); \qquad \delta^{\mathrm{up}} = 0.75 \times 10^{-4}\ \mathrm{m}^{-1}, \tag{A.2}$$

whereas turbulent detrainment rates for shallow convection are set proportional to the entrainment rates

$$D^{\mathrm{up}}_{\mathrm{shal}} = E^{\mathrm{up}}_{\mathrm{shal}}\Big(1.6 - RH\Big). \tag{A.3}$$

In addition, when the updraft becomes negatively buoyant, organized detrainment is applied. It is estimated by equating the decrease in updraft vertical kinetic energy at the top of the cloud to the decrease in mass flux with height.

Downdraft turbulent detrainments are set equal to the downdraft entrainment rates, while organized detrainment is enforced over the lowest 50 hPa.

References

Ahlgrimm, M. and R. Forbes, 2012: The impact of low clouds on surface shortwave radiation in the ecmwf model. *Mon. Weather Rev.*, **140**, 3783–3794.

Arakawa, A. and W. Schubert, 1974: Interaction of a cumulus ensemble with the large-scale environment. Part I. *J. Atmos. Sci.*, **31**, 674–701.

Bechtold, P., J.-P. Chaboureau, A. Beljaars, A. K. Betts, M. Köhler, M. Miller, and J.-L. Redelsperger, 2004: The simulation of the diurnal cycle of convective precipitation over land in global models. *Q. J. R. Meteorol. Soc.*, **130**, 3119–3137.

Bechtold, P., M. Köhler, T. Jung, F. Doblas-Reyes, M. Leutbecher, M. Rodwell, F. Vitart, and G. Balsamo, 2008: Advances in simulating atmospheric variability with the ECMWF model: From synoptic to decadal time-scales. *Q. J. R. Meteorol. Soc.*, **134**, 1337–1351.

Benedict, J. J., A. Sobel, D. M. W. Frierson, and L. J. Donner, 2013: Tropical Intraseasonal Variability in Version 3 of the GFDL Atmosphere Model. *J. Climate*, **26(2)**, 426–449.

Betts, A. K. and C. Jakob, 2002: Study of diurnal cycle of convective precipitation over Amazonia using a single column model. *J. Geophys. Res.*, **107**, 1–13, doi:10.1029/2002JD002 264.

Betts, A. K. and M. J. Miller, 1986: A new convective adjustmentscheme. Part II: Single column tests using GATE-wave, BOMEX, ATEX, and Arctic Airmass data sets. *Q. J. R. Meteorol. Soc.*, **112**, 693–710.

Blackburn, M., et al., 2013: The Aqua Planet Experiment (APE): CONTROL SST Simulation. *J. Meteorol. Soc. Jpn*, **91A**, doi:10.2151/jmsj.2013–A02.

Bougeault, P., 1985: A simple parameterization of the large-scale effects of cumulus convection. *Mon. Weather Rev.*, **113**, 2108–2121.

Brockhaus, P., D. Lüthi, and C. Schär, 2008: Aspects of the diurnal cycle in a regional climate model. *Meteorol. Zeitschr.*, **17**, 433–443.

Chaboureau, J.-P., F. Guichard, J.-L. Redelsperger, and J.-P. Lafore, 2004: The role of stability and moisture in the diurnal cycle of convection over land. *Q. J. R. Meteorol. Soc.*, **130**, 3105–3117.

Clark, A. J., W. A. G. Jr., and T.-C. Chen, 2007: Comparison of the diurnal precipitation cycle in convection-resolving and non-convection-resolving mesoscale models. *Mon. Weather Rev.*, **135**, 3456–3473.

Craig, G. C., 1996: Dimensional analysis of a convecting atmosphere in equilibrium with external forcing. *Q. J. R. Meteorol. Soc.*, **122**, 1963–1967.

Dai, A., F. Giorgi, and K. E. Trenberth, 1999: Observed and model simulated diurnal cycles of precipitation over the contiguous united states. *J. Geophys. Res.*, **104**, 6377–6402.

Davies, L., R. S. Plant, and S. H. Derbyshire, 2013: Departures from convective equilibrium with a rapidly-varying surface forcing. *Q. J. R. Meteorol. Soc.*, doi: 10.1002/qj.2065.

de Rooy, W., P. Bechtold, K. Fröhlich, C. Hohenegger, H. Jonker, S. Mironov, J. Teixeira, and J.-I. Yano, 2013: Entrainment and detrainment in cumulus convection: An overview. *Q. J. R. Meteorol. Soc.*, **139**, 1–19.

Del Genio, A. D. and J. Wu, 2010: The role of entrainment in the diurnal cycle of continental convection. *J. Climate*, **23**, 2722–2738.

Derbyshire, S. H., I. Beau, P. Bechtold, J.-Y. Grandpeix, J.-M. Piriou, J.-L. Redelsperger, and P. M. M. Soares, 2004: Sensitivity of moist convection to environmental humidity. *Q. J. R. Meteorol. Soc.*, **130**, 3055–3080.

Donner, L. J. and V. T. Philips, 2003: Boundary-layer control on convective available potential energy: Implications for cumulus parametrization. *J. Geophys. Res.*, **108.4701**, doi:10.1029/2003JD003 773.

Emanuel, K. A., 1993a: The effect of convective response time on wishe modes. *J. Atmos. Sci.*, **50**, 1763–1775.

Emanuel, K. A., 1993b: A scheme for representing cumulus convection in large scale models. *J. Atmos. Sci.*, **48**, 2313–2335.

Emanuel, K. A., J. D. Neelin, and C. S. Bretherton, 1994: On large-scale circulations in convecting atmospheres. *Q. J. R. Meteorol. Soc.*, **120**, 1111–1143.

Fletcher, J. K. and C. S. Bretherton, 2010: Evaluating boundary-layer based mass flux closures using cloud-resolving model simulations of deep convection. *J. Atmos. Sci.*, **67**, 2212–2225.

Fritsch, J. M. and C. G. Chappell, 1980: Numerical prediction of convectively driven mesoscale pressure systems. Part I: Convective parametrization. *J. Atmos. Sci.*, **37**, 1722–1733.

Fuchs, Z. and D. Raymond, 2007: A simple, vertically resolved model of tropical disturbances with a humidity closure. *Tellus*, **59A**, 344–354.

Gerard, L., J.-M. Piriou, R. Brozková, J.-F. Geleyn, and D. Banciu, 2009: Cloud and precipitation parameterization in a meso-gamma-scale operational weather prediction model. *Mon. Weather Rev.*, **137**, 3960–3977.

Grabowski, W. W., et al., 2006: Daytime convective development over landÂ : an idealized model intercomparison based on LBA observations. *Q. J. R. Meteorol. Soc.*, **133**, 317–344.

Gregory, D., J.-J. Morcrette, C. Jacob, A. C. M. Beljaars, and T. Stockdale, 2000: Revision of convection, radiation and cloud schemes in the ecmwf integrated forecasting system. *Q. J. R. Meteorol. Soc.*, **126**, 1685–1710.

Gregory, D. and P. R. Rowntree, 1990: A mass flux convection scheme with representation of cloud ensemble characteristics and stability-dependent closure. *Mon. Weather Rev.*, **118**, 1483–1506.

Guichard, F., et al., 2004: Modelling the diurnal cycle of deep precipitating convection over land with CRMs and SCMs. *Q. J. R. Meteorol. Soc.*, **130**, 3139–3172.

Hirons, L., P. Inness, F. Vitart, and P. Bechtold, 2013a: Understanding advances in the simulation of intraseasonal variability in the ECMWF model. Part I: The representation of the MJO. *Q. J. R. Meteorol. Soc.*, DOI: 10.1002/qj.2059.

Hirons, L., P. Inness, F. Vitart, and P. Bechtold, 2013b: Understanding advances in the simulation of intraseasonal variability in the ECMWF model. Part II: The application of process-based diagnostics. *Q. J. R. Meteorol. Soc.*, DOI: 10.1002/qj.2060.

Jones, T. R. and D. A. Randall, 2011: Quantifying the limits of convective parametrizatons. *J. Geophys. Res.*, **106**, D08 210.

Jung, T., et al., 2010: The ECMWF model climate: recent progress through improved physical parametrizations. *Q. J. R. Meteorol. Soc.*, **136**, 1145–1160.

Kain, J. S. and J. M. Fritsch, 1993: Convective parameterization for mesoscale models: the Kain-Fritsch Scheme. *Meteorol. Monogr.*, **46**, 165–170.

Khairoutdinov, M. and D. A. Randall, 2006: High-resolution simulations of shallow-to-deep convection transition over land. *J. Atmos. Sci.*, **63**, 3421–3436.

Kim, D., A. H. Sobel, E. D. Maloney, D. M. W. Frierson, and L.-S. Kang, 2011: A systematic relationship between intraseasonal variability and mean state bias in agcm simulations. *J. Climate*, **24**, 5506–5520.

Lafore, J.-P., et al., 1998: The Meso–NH Atmospheric Simulation System. Part I: adiabatic formulation and control simulations. Scientific objectives and experimental design. *Ann. Geophys.*, **16**, 90–109.

Langhans, W., J. Schmidli, O. Fuhrer, S. Bieri, and C. Schär, 2013: Long-term simulations of thermally-driven flows and orographic convection at convection-parameterizing and cloud-resolving resolutions. e–view.

Langhans, W., J. Schmidli, and C. Schär, 2012: Bulk convergence of cloud-resolving simulations of moist convection over complex terrain. *J. Atmos. Sci.*, **69**, 2207–2228.

Lin, J. L., et al., 2006: Tropical intraseasonal variability in 14 IPCC AR4 climate models. Part I: Convective signals. *J. Climate*, **19**, 2665–2690.

Lin, Y. and K. E. Mitchell, 2005: The NCEP Stage II/IV Hourly Precipitation Analyses: Development and Applications. *Proceedings of the 19th AMS Conference on Hydrology, San Diego, CA (USA), 5–14 January 2005*.

Lin, Y., et al., 2012: TWP-ICE global atmospheric model intercomparison: convection responsiveness and resolution impact. *J. Geophys. Res.*, **117**, D09 111,doi:10.1029/2011JD017 018.

Mapes, B. E., 2000: Convective inhibition, subgrid-scale triggering energy, and stratiform instability in a toy tropical wave model measurements. *J. Atmos. Sci.*, **57**, 1515–1535.

Marsham, J. H., N. Dixon, L. Garcia-Carreras, D. J. P. M. S. Grenville. Lister, P. Knippertz, and C. Birch, 2013: The role of moist convection in the west african monsoon system. insights from continental-scale convection-permitting simulations. *Geophys. Res. Let.*, available online.

Mathon, V., H. Laurent, and T. Lebel, 2003: Mesoscale convective system rainfall in the Sahel. *J. Appl. Meteor. Climat.*, **41**, 1081–1092.

Neelin, J. D. and J.-Y. Yu, 1994: Modes of tropical variability under convective adjustment and the Madden-Julian oscillation. Part I: Analytical theory. *J. Atmos. Sci.*, **51**, 25–42.

Nesbitt, S. W. and E. J. Zipser, 2003: The diurnal cycle of rainfall and convective intensity according to three years of TRMM measurements. *J. Climate*, **16**, 1456–1475.

Nordeng, T.-E., 1994: Extended versions of the convection parametrization scheme at ECMWF and their impact upon the mean climate and transient activity of the model in the tropics. *ECMWF Tech. Memo. No. 206*.

Pan, D.-M. and D. A. Randall, 1998: A cumulus parameterization with prognostic closure. *Q. J. R. Meteorol. Soc.*, **124**, 949–981.

Parker, D. J., 2002: The response of CAPE and CIN to tropospheric thermal variations. *Q. J. R. Meteorol. Soc.*, **128**, 119–130.

Petch, J. C., A. R. Brown, and M. E. B. Gray, 2002: The impact of horizontal resolution on the simulations of convective development over land. *Q. J. R. Meteorol. Soc.*, **28**, 2031–2044.

Piriou, J.-M., J.-L. Redelsperger, J.-F. Geleyn, J.-P. Lafore, and F. Guichard, 2007: An approach for convective parameterization with memory, in separating microphysics and transport in grid-scale equations. *J. Atmos. Sci.*, **64**, 4127–4139.

Raymond, D. J., 1995: Regulation of moist convection over the west pacific warm pool. *J. Atmos. Sci.*, **52**, 3945–3959.

Raymond, D. J. and M. J. Herman, 2011: Convective quasi-equilibrium reconsidered. *J. Adv. Model. Earth Sys.*, **3**, M08 003,14.

Rio, C., F. Hourdin, J.-Y. Grandpeix, and J. P. Lafore, 2009: Shifting the diurnal cycle of parameterized deep convection over land. *Geophys. Res. Let.*, **36**, L07 809,doi:10.1029/2008GL036 779.

Sato, T., H. Miura, M. Satoh, Y. N. Takayabu, and Y. Wang, 2009: Diurnal cycle of precipitation in the tropics simulated in a global cloud-resolving model. *J. Climate*, **22**, 4809–4826.

Sato, T., T. Yoshikane, M. Satoh, H. Miura, and H. Fujinami, 2008: Resolution dependency of the diurnal cycle of convective clouds over the tibetan plateau in a mesoscale model. *J. Meteorol. Soc. Jpn*, **86A**, 17–31.

Schlemmer, L., C. Hohenegger, J. Schmidli, C. Bretherton, and C. Schär, 2011: An idealized cloud-resolving framework for the study of summertime midlatitude diurnal convection over land. *Q. J. R. Meteorol. Soc.*, **68**, 1041–1057.

Shutts, G. J. and M. E. B. Gray, 1999: Numerical simulations of convective equilibrium under prescribed forcing. *Q. J. R. Meteorol. Soc.*, **125**, 2767–2787.

Slingo, J. M., K. Sperber, J.-J. Morcrette, and G. L. Potter, 1992: Analysis of the temporal behavior of convection in the tropics of the European Centre for Medium-range Weather Forecast model. *J. Geophys. Res.*, **97**, 119–135.

Stirling, A. and R. A. Stratton, 2012: Entrainment processes in the diurnal cycle of deep convection over land. *Q. J. R. Meteorol. Soc.*, **138**, 1135–1149.

Stratton, R. A. and A. Stirling, 2012: Improving the diurnal cycle of convection in gcms. *Q. J. R. Meteorol. Soc.*, **138**, 1121–1134.

Takayabu, Y. and M. Kimoto, 2008: Diurnal march of rainfall simulated in a T106 AGCM and dependence on cumulus schemes. *J. Meteorol. Soc. Jpn*, **86A**, 163–173.

Tian, B., I. M. Held, N.-C. Lau, and B. J. Soden, 2005: Diurnal cycle of summertime deep convection over North America: A satellite perspective. *J. Geophys. Res.*, **110**, 1–10, doi:10.1029/2004JD005 275.

Tiedtke, M., 1989: A comprehensive mass flux scheme for cumulus parametrization in large-scale models. *Mon. Weather Rev.*, **117**, 1779–1800.

Vitart, F. and F. Molteni, 2009: Simulation of the MJO and its teleconnections in an ensemble of 46-day hindcasts. *Q. J. R. Meteorol. Soc.*, **136**, 842–856.

Yang, G.-Y. and J. Slingo, 2001: The diurnal cycle in the tropics. *Mon. Weather Rev.*, **129**, 784–801.

Yano, J.-I., M. Bister, Z. Fuchs, L. Gerard, V. Phillips, S. Barkidija, and J.-M. Piriou, 2013: Phenomenology of convection-parameterization closure. *Atmos. Chem. Phys.*, doi:10.5194/acpd–12–25 743–2012.

Yano, J.-I. and R. Plant, 2012: Finite departures from convective quasi-equilibrium: periodic cycle and discharge-recharge mechanism. *Q. J. R. Meteorol. Soc.*, **138**, 626–637.

Zhang, G. J., 2002: Convective quasi-equilibrium in midlatitude continental environment and its effect on convective parameterization parametrization. *J. Geophys. Res.*, **107**, doi:10.1029/2001JD001 005.

Zhang, G. J. and N. A. McFarlane, 1995: Sensitivity of climate simulations to the parameterization of cumulus convection in the Canadian climate centre general circulation model. *Atmosphere-Ocean*, **33**, 407–446.

Zhang, Y. and S. A. Klein, 2010: Mechanisms affecting the transition from shallow to deep convection over land: Interferences from observations of the diurnal cycle collected at the ARM Southern Great Plains site. *J. Atmos. Sci.*, **67**, 2943–2959.

Zhang, Y. and S. A. Klein, 2013: Factors controlling the vertical extent of fair-weather shallow cumulus clouds over land: Investigation of diurnal-cycle observations collected at the arm southern great plains site. *J. Atmos. Sci.*, **70**, 1297–1315.

Zimmer, M., G. C. Craig, C. Keil, and H. Wernli, 2011: Classification of precipitation events with a convective response timescale and their forecasting characteristics. *Geophys. Res. Let.*, **38**, L05 802.